Innovation and Technology Studies
Print ISSN: 3007-6919
Online ISSN: 3007-6927
DOI: https://doi.org/10.61784/its4027

MOMENT-CONSTRAINED SIDE-FORCE ALLOCATION FOR WIND-ASSISTED MERCHANT SHIPS: HYDRODYNAMIC PERFORMANCE OF RETRACTABLE ANTI-LEEWAY FINS AND FLAP RUDDERS

FuYong Zhou
StormGeo, Shanghai 200003, China.

Abstract: Wind-assisted propulsion generates an aerodynamic side force and yaw moment that must be balanced hydrodynamically through leeway, helm and appendage loading. Retractable anti-leeway fins with adjustable incidence and flap rudders are being introduced for this purpose, but their benefit for large merchant ships has not been quantified with a method that resolves the coupled side-force and yaw-moment allocation. This paper develops a moment-constrained side-force allocation framework and applies it to the KVLCC2 tanker fitted with four wing sails. The framework couples (i) captive-test-based manoeuvring (MMG) coefficients for hull, propeller and rudder, (ii) a low-aspect-ratio lifting-surface model for fins and flap rudders that combines a vortex-lattice method with a reflection plane, XFOIL section polars at full-scale Reynolds number and a cross-flow non-linearity, (iii) hull up-wash, boundary-layer immersion and fin–rudder vortex interaction, and (iv) a joint optimisation of sail trim, leeway, helm, flap angle, fin incidence and fin deployment. A closed-form result is derived for the minimum side-force cost, together with the yaw-balance capacity and the break-even side force for fin deployment. The theory reproduces the non-linear optimum within 1.7% and predicts the fin break-even side force (1.92 MN) within 2.1%. Route-level evaluation with two real wind datasets (NOAA buoy 46002 and the NREL WIND Toolkit) shows that, at a sail-area ratio of 0.6, 12 kn and a 10° helm limit, all appendage options change annual savings by less than 0.05 percentage points while a flap rudder reduces the time spent above 8° helm from 1.96% to 0.35%. When yaw balance becomes binding (sail-area ratio 1.2, 10 kn, 5° helm limit), the flap rudder adds 4.66 points to a 40.0% baseline saving, a retractable adjustable fin adds 3.52 points and the combination adds 4.77 points with the fin deployed 16% of the time (Monte Carlo: 4.83 ± 0.56 points). Neglecting propeller unloading overstates the baseline saving by 2.0 points, and sail-first trimming loses 0.83 points relative to joint optimisation.
Keywords: Wind-assisted ship propulsion; Anti-leeway fin; Flap rudder; Yaw balance; Side-force allocation; MMG model; Vortex-lattice method; KVLCC2

1 INTRODUCTION

The 2023 IMO Strategy on Reduction of GHG Emissions from Ships commits international shipping to net-zero greenhouse-gas emissions by or around 2050, with intermediate reduction checkpoints in 2030 and 2040 [1]. Wind-assisted ship propulsion (WASP) is one of the few technologies that can be retrofitted to the existing fleet and that reduces fuel consumption without changing the fuel supply chain [2]. Performance-prediction studies report substantial savings for tankers and roll-on/roll-off ships on realistic routes, and they show that the predicted savings depend on the aero- and hydrodynamic interaction model used [3].

Every lift-based wind propulsor produces, besides thrust, a side force and a yaw moment. In steady operation these loads are balanced by the hull, which sails with a leeway angle, and by the rudder, which operates with a steady helm angle. The hull of a merchant ship behaves as a very low-aspect-ratio lifting body whose centre of lateral resistance lies far forward, so the side force is accompanied by a destabilising hydrodynamic yaw moment [4, 5]. Towing-tank experiments on systematic hull series and appendages have shown that bilge keels can mitigate this yaw moment and promote non-linear side force [6, 7]. A systematic analysis of a wind-powered cargo ship found that the sail-induced resistance can be comparable to the added resistance in waves, that the rudder operating at large steady angles is its main source, and that among fixed and dynamic keels only the dynamically controlled keel significantly improved the fuel savings [8].

Two families of devices address these mechanisms directly. Retractable anti-leeway fins (daggerboards) with adjustable fin angle have recently been introduced for ships equipped with wind-assisted propulsion systems [9]. Flap rudders increase the rudder lift obtained per unit helm angle and are an established option for improving manoeuvring capability [10, 11]. Both devices act on the same pair of equilibrium conditions—sway force and yaw moment—and therefore compete with, and complement, the side force that the hull produces at leeway and the rudder produces at helm.

The design question addressed here is when, and by how much, such devices improve the propulsive power of a wind-assisted merchant ship. Three gaps prevent a quantitative answer. First, appendage studies usually assess each device as a fixed addition and judge it by the resulting drift or resistance, while the actual mechanism is an allocation of side force and yaw moment among several lifting elements whose loading can be controlled. Second, the rudder inflow of a wind-assisted ship depends on propeller loading, which decreases as the sails take over thrust, so the rudder's capacity to

© By the Author(s) 2026, under the CC BY-NC-ND license (http://creativecommons.org/licenses/by-nc-nd/4.0).

balance yaw shrinks exactly when the aerodynamic loads are largest. Third, benefits must be integrated over realistic wind statistics, including a deployment policy for retractable devices, before a design decision can be made.

This paper formulates the hydrodynamic balance of a wind-assisted ship as a moment-constrained side-force allocation problem and makes four contributions.

1. A linear-quadratic allocation theory that gives the minimum side-force cost in closed form, $D^* = F^2/(2K)\left[1 + \left((x_A - \bar{x})/\sigma\right)^2\right]$, in terms of three invariants of the appendage system (side-force conductance K, hydrodynamic centre $\bar{x}$ and lever spread σ), the yaw-balance capacity under helm limits, and the break-even side force above which deploying a fin pays.
2. A mid-fidelity hydrodynamic model for low-aspect-ratio fins and flap rudders—vortex-lattice lift slope with a reflection plane, XFOIL section polars at full-scale Reynolds number and a cross-flow non-linearity—coupled to captive-test-based MMG coefficients of the KVLCC2 hull, propeller and rudder, including hull up-wash, boundary-layer immersion and fin–rudder vortex interaction.
3. A joint optimal-operation formulation that trims the sails together with leeway, helm, flap angle, fin incidence and fin deployment, compared against the sail-first practice of trimming for maximum thrust and then balancing the ship.
4. A route-level evaluation with two independent real wind datasets, supported by regime maps, fin design maps, ablations and Monte Carlo robustness analysis, which identifies the operating regimes in which fins and flap rudders pay.

Section 2 states the equilibrium and optimisation problem, Section 3 the hydrodynamic and aerodynamic models, and Section 4 the allocation theory. Section 5 describes the data and experimental design, Section 6 presents the results, Section 7 discusses design implications and Section 8 concludes.

2 PROBLEM FORMULATION

2.1 Steady Sailing Equilibrium

A ship-fixed frame is used with x forward, y to starboard and the origin at midship. The ship advances along its course at speed V; the leeway (drift) angle follows the MMG convention $\beta = \tan^{-1}(-v/u)$ with $u = V\cos\beta$, $v = -V\sin\beta$ [12]. In steady straight sailing the surge, sway and yaw equilibria read

$$\begin{aligned} (1 - t_P)\,T + X_H + X_R + X_F + X_A &= 0, \\ Y_H + Y_R + Y_F + Y_A &= 0, \\ N_H + N_R + N_F + N_A &= 0, \end{aligned} \tag{1–3}$$

where subscripts H, R, F and A denote hull, rudder, anti-leeway fin and aerodynamic (sail) loads, T is the propeller thrust and t_P the thrust-deduction factor. Heel is not modelled: the KVLCC2 displaces about 3.2×10^5 t, and a heeling moment of 80 MNm (2 MN side force at 40 m lever) produces less than 0.3° of heel for a metacentric height of the order of 5 m. Figure 1 summarises the force system.

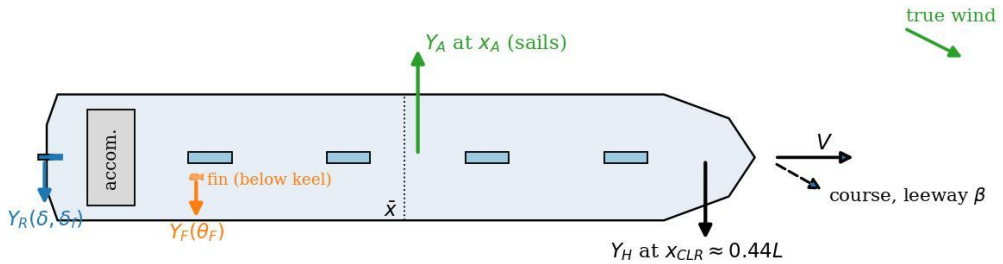


Figure 1 Plan View of the Side-Force System: Sail Side Force Y_A at the Centre of Effort x_A, Hull Force Y_H Acting near the Centre of Lateral Resistance ($\approx 0.44L$ Forward of Midship for KVLCC2), Anti-Leeway Fin Force Y_F Controlled by Incidence θ_F, and Rudder Force Y_R Controlled by Helm δ and Flap Angle δ_f. $\bar{x}$ marks the hydrodynamic centre of the appendage system defined in Section 4.

2.2 Optimal Operation Problem

For given true wind speed at 10 m height U_{10} and true wind angle relative to the course TWA, the operating point is obtained from

$$\begin{aligned} &\min_{\mathbf{z},\,\chi} \quad P_D(\mathbf{z}, \chi) \\ &\text{s.t.} \quad \text{Eqs. (1)–(3)}, \qquad |\delta| \le \delta_{\max}, \qquad |\beta| \le \beta_{\max}, \\ &C_{L,k} \in \left[m\,C^-_{L,k}(\delta_k),\ m\,C^+_{L,k}(\delta_k)\right], \quad k \in \{R, F, A\}, \end{aligned} \tag{4}$$

with decision vector $\mathbf{z} = (\beta, \delta, T, \theta_F, \delta_f, \alpha_s, \delta_s)$, where θ_F is the fin incidence, δ_f the rudder flap angle, α_s the sail angle of attack and δ_s the sail flap angle. The binary variable χ indicates whether the retractable fin is deployed, and

P_D is the delivered power. The lift coefficients of rudder, fin and sails are kept within a margin $m = 0.9$ of their attached-flow limits $C_{L,k}^{\pm}$, which depend on the flap angle. The helm limit $\delta_{\max}$ represents the steering reserve kept for course keeping; $\delta_{\max} = 10^{\circ}$ is the baseline and 5°–15° are examined. $\beta_{\max} = 10^{\circ}$ bounds the leeway to the range covered by the manoeuvring coefficients.

2.3 Configurations

Six configurations are compared (Table 1). C0 is the reference wind-assisted ship with a conventional rudder; C1 and C2 replace it by a flap rudder of identical area whose flap is either mechanically linked ($\delta_f = k\,\delta,\ k = 1$) or independently controlled; C3 and C4 add an anti-leeway fin with fixed or adjustable incidence; and C5 combines the adjustable fin with the independently controlled flap rudder. Because the fin is retractable, C3–C5 are reported both with the fin permanently deployed and with the optimal deployment policy, which retracts the fin whenever this lowers P_D (retracted C3/C4 equal C0, retracted C5 equals C2).

Table 1 Configurations and Their Control Variables

Config.	Rudder	Fin	Controls besides $(\beta, \delta, T, \alpha_s, \delta_s)$
C0	conventional	–	–
C1	flap, linked $\delta_f = \delta$	–	–
C2	flap, independent	–	δ_f
C3	conventional	fixed, $\theta_F = 0$	deployment χ
C4	conventional	adjustable	$\theta_F,\ \chi$
C5	flap, independent	adjustable	$\theta_F,\ \delta_f,\ \chi$

3 HYDRODYNAMIC AND AERODYNAMIC MODELS

3.1 Hull and Calm-Water Resistance

Hull forces follow the MMG standard method with the KVLCC2 coefficients obtained from captive model tests (Table 2) [12]; the values were cross-checked against an open implementation of the method [13]. For straight sailing ($r = 0$) and $v' = -\sin\beta$,

$$\begin{aligned} X_H &= 1/2\,\rho V^2 L d\left(X'_{vv}v'^2 + X'_{vvvv}v'^4\right) - R_T(V), \\ Y_H &= 1/2\,\rho V^2 L d\left(Y'_{v}v' + Y'_{vvv}v'^3\right), \\ N_H &= 1/2\,\rho V^2 L^2 d\left(N'_{v}v' + N'_{vvv}v'^3\right). \end{aligned} \tag{5}$$

The full-scale calm-water resistance is $R_T = 1/2\,\rho S V^2\left[(1+k)C_F + C_A\right]$ with the ITTC-1957 friction line $C_F = 0.075/\left(\log_{10}Re - 2\right)^2$, the Holtrop–Mennen form factor

$$\begin{aligned} 1 + k = \ & 0.93 + 0.487118(B/L)^{1.06806}(T/L)^{0.46106} \\ & \times (L/L_R)^{0.121563}(L^3/\nabla)^{0.36486}(1 - C_P)^{-0.604247} \end{aligned} \tag{6}$$

and the correlation allowance $C_A = 0.006(L + 100)^{-0.16} - 0.00205$ [14]. With the KVLCC2 particulars this gives $1 + k = 1.322$, $R_T = 803$ kN at 10 kn and 1134 kN at 12 kn ($F_n \le 0.11$, where wave-making resistance is negligible) [15].

Table 2 KVLCC2 Main Particulars [15] and MMG Coefficients Used [12]

Quantity	Value	Coefficient	Value
$L_{pp},\ B,\ d,\ D$	320, 58, 20.8, 30.0 m	$Y'_v,\ Y'_{vvv}$	$-0.315, -1.607$
$\nabla,\ S$	312 621 m³, 27 194 m²	$N'_v,\ N'_{vvv}$	$-0.137, -0.030$
C_B, LCB	0.8098, $+3.48\%L$	$X'_{vv},\ X'_{vvvv}$	$-0.040, 0.771$
$D_P,\ H_R,\ A_R$	9.86 m, 15.8 m, 112.6 m²	$t_P,\ w_{P0}$	0.220, 0.40
$1 + k$ (Eq. 6)	1.322	$t_R,\ a_H,\ x'_H$	0.387, 0.312, -0.464
$P_{D,\mathrm{ref}}$ at 10/12 kn	5.87/9.90 MW	$\gamma_R^-,\ \gamma_R^+,\ x'_R$	0.395, 0.640, -0.500
		$\varepsilon,\ \kappa,\ f_\alpha$	1.09, 0.50, 2.747
		$k_0,\ k_1,\ k_2$	0.2931, -0.2753, -0.1385

3.2 Propeller and Rudder Inflow

The propeller operates at $J = u_P/(nD_P)$ with $K_T = k_0 + k_1 J + k_2 J^2$, inflow $u_P = V\cos\beta\,(1 - w_P)$ and $w_P = w_{P0}\exp(-4\beta^2)$ [12]. For a required thrust T, the loading $K_T/J^2 = T/(\rho D_P^2 u_P^2)$ fixes J through the quadratic $K_T(J)$. The delivered power is computed from actuator-disc theory, $P_D = T u_P/(\zeta \eta_i)$ with $\eta_i = 2/\left(1 + \sqrt{1 + 8K_T/(\pi J^2)}\right)$ and a constant blade-friction factor $\zeta = 0.8$ that cancels in all relative savings. The rudder inflow follows the MMG slipstream model

$$u_R = \varepsilon u_P \sqrt{\eta\{1 + \kappa\left(\sqrt{1 + 8K_T/\pi J^2} - 1\right)\}^2 + (1 - \eta)}, \qquad v_R = V\gamma_R(\beta)\,\beta + v_F, \tag{7}$$

with $\eta = D_P/H_R$. The flow-straightening coefficient switches between γ_R^- and γ_R^+ with the sign of β; it is smoothed as $\gamma_R = \bar{\gamma}_R + \Delta\gamma_R \tanh(\beta/0.5^\circ)$ for gradient-based optimisation. The term v_F is the sidewash induced by the fin (Section 3.5). Equation (7) makes the rudder dynamic pressure decrease as the sails unload the propeller, which is the coupling examined in the ablation study.

3.3 Section Polars with Plain Flaps

Section characteristics were computed with XFOIL 6.99 at full-scale Reynolds numbers: NACA 0018 with a 20%, 30% or 40% chord plain flap at $Re = 3 \times 10^7$ for the rudder, NACA 0015 at $Re = 3 \times 10^7$ for the fin, NACA 0018 with a 30% flap at $Re = 1.5 \times 10^7$ for the wing sails, and NACA 0015 at $Re = 2.7 \times 10^6$ for validation [16]. Flap deflections of 0–30° in 5° steps were analysed with the deflected geometry and $N_{\mathrm{crit}} = 9$; negative deflections follow from section symmetry. Each polar is condensed into a smooth parametric representation

$$c_l = a_0(\delta_f)\left(\alpha + \Delta\alpha_0(\delta_f)\right), \qquad c_d = c_0(\delta_f) + c_1(\delta_f)\,c_l + c_2(\delta_f)\,c_l^2, \tag{8}$$

with the attached-flow limits $c_l^{\pm}(\delta_f)$; the parameters are spline-interpolated in δ_f. The zero-lift shift $\Delta\alpha_0$ defines the viscous flap effectiveness $\tau = \Delta\alpha_0/\delta_f$. NeuralFoil provides an independent set of polars for the robustness study [17].

3.4 Low-Aspect-Ratio Lifting Surfaces

Rudder, fin and sails are low-aspect-ratio surfaces mounted on, or close to, a reflecting boundary. Their lift slope and induced-drag factor are computed with a vortex-lattice method (VLM) using horseshoe vortices, cosine spanwise spacing and a Trefftz-plane drag evaluation [18]; the hull bottom (fin) or the deck (sails, with a 3 m gap) is represented by an image surface. The three-dimensional coefficients are

$$\begin{aligned} C_L &= C_{L\alpha}\,\alpha_e + \frac{C_{DC}}{\Lambda_e}\,\alpha_e|\alpha_e|, \qquad \alpha_e = \alpha + \Delta\alpha_0(\delta_f), \\ C_D &= c_d(C_L, \delta_f) + K_i\,C_L^2, \\ C_{L\alpha} &= C_{L\alpha}^{\mathrm{VLM}}\,\frac{\mathcal{H}(a_0,\Lambda_e)}{\mathcal{H}(2\pi,\Lambda_e)}, \qquad \mathcal{H}(a,\Lambda) = \frac{a\Lambda}{a/\pi + \sqrt{\Lambda^2 + (a/\pi)^2}}, \end{aligned} \tag{9}$$

where Λ_e is the effective aspect ratio including the image, K_i the VLM induced-drag factor and $\mathcal{H}$ the Helmbold relation used to transfer the viscous section slope a_0 to three dimensions. The cross-flow term with $C_{DC} = 0.8$ for square tips is the non-linearity identified by Whicker and Fehlner for low-aspect-ratio control surfaces [19]. A full-span flap shifts the effective angle by the viscous $\Delta\alpha_0$, which is consistent with the VLM ratio of flap to angle-of-attack effectiveness (Section 6.1). For the rudder, $C_{L\alpha}$ is anchored to the measured MMG normal-force gradient $f_\alpha = 2.747$ so that the conventional rudder reproduces the captive-test data; the flap rudder differs from it only through the flap terms of Eqs. (8)–(9).

The rudder lift and drag act normal and parallel to the local inflow angle $\varphi_R = -\tan^{-1}(v_R/u_R)$, with $\alpha_R = \delta + \varphi_R$ and $q_R = 1/2\,\rho(u_R^2 + v_R^2)$:

$$\begin{aligned} X_r &= L_R\sin\varphi_R - D_R\cos\varphi_R, \qquad Y_r = -\left(L_R\cos\varphi_R + D_R\sin\varphi_R\right), \\ X_R &= (1 - t_R)X_r, \qquad Y_R = (1 + a_H)Y_r, \qquad N_R = (x'_R + a_H x'_H)\,L\,Y_r. \end{aligned} \tag{10}$$

3.5 Anti-Leeway Fin

The fin is a retractable daggerboard of span s_F (depth below the keel) and chord c_F, mounted on the flat bottom at x_F. Under a drifting hull the lateral flow is accelerated around the bilges. Modelling the double-body midship section as an ellipse with semi-axes $a = B/2$ and $b = d$, the lateral velocity ratio on the vertical symmetry line at depth h below the keel follows from the Joukowski mapping $\xi = \zeta + c^2/\zeta$ with $c^2 = (a^2 - b^2)/4$ and $R = (a + b)/2$:

$$\frac{u_y(h)}{V\sin\beta} = \mathrm{Re}\left[\frac{1 - R^2/\zeta^2}{1 - c^2/\zeta^2}\right]_{\xi = -\mathrm{i}(b+h)}, \qquad \kappa_F = \frac{\int_0^{s_F} \frac{u_y}{V\sin\beta}\,w\,\mathrm{d}h}{\int_0^{s_F} w\,\mathrm{d}h}, \quad w = \sqrt{1 - (h/s_F)^2}, \tag{11}$$

which gives $1 + b/a = 1.72$ at the keel. The dynamic pressure is reduced by immersion in the turbulent hull boundary layer (1/7 power law, flat-plate thickness at x_F). The fin angle of attack is $\alpha_F = \theta_F - \tan^{-1}(\kappa_F \tan\beta)$, and the fin lift and drag are tilted by the undisturbed inflow angle,

$$X_F = -L_F \sin\beta - D_F \cos\beta, \qquad Y_F = -(L_F \cos\beta - D_F \sin\beta), \qquad N_F = x_F Y_F, \tag{12}$$

so that up-wash raises the fin loading without producing an unphysical thrust from the locally rotated flow. The fin tip vortex, of strength $\Gamma_F = 4|L_F|/(\pi \rho V s_F)$ for elliptic loading, is convected along the free stream to the rudder station, where it lies at depth $d + \pi s_F/4$ and lateral offset $y_v = (x_F - x_R)\tan\beta$. Its sidewash at rudder mid-span,

$$v_F = -\operatorname{sgn}(Y_F)\, \frac{\Gamma_F \Delta z}{2\pi (y_v^2 + \Delta z^2)}, \tag{13}$$

with Δz the vertical distance between vortex and rudder mid-span, reduces the rudder inflow angle when the fin and rudder carry side force of the same sign.

3.6 Wing Sails and Wind

Four rigid wing sails (span 50 m, chord 20 m, NACA 0018 with a 30% flap) are placed on the deck at $x/L = 0.32$, 0.12, -0.08 and -0.28, giving $A_S = 4000$ m², $A_S/(Ld) = 0.60$ and a centre of effort $x_A = 0.02L$. The sails share a common trim (α_s, δ_s); sail–sail interaction is not modelled. Their coefficients follow Eq. (9) with the deck image ($\Lambda_e = 5.0$), no cross-flow term and a parasitic drag of 0.005. The true wind at the sail centroid ($z_c = 37.2$ m above the waterline) follows the offshore power law $U(z) = U_{10}(z/10)^{0.11}$ [20]. The apparent wind $\mathbf{A}$ is the true-wind velocity minus the ship velocity, both expressed in the hull frame rotated by the leeway; lift acts normal to $\mathbf{A}$ and drag along it, so the sail thrust in the hull frame already contains the course-projection loss caused by leeway.

4 MOMENT-CONSTRAINED SIDE-FORCE ALLOCATION THEORY

4.1 Linear-Quadratic Formulation

Consider an aerodynamic side force F acting normal to the course at the centre of effort $x_A L$. Let $\mathbf{u} \in \mathbb{R}^n$ collect the hydrodynamic control variables, e.g. $\mathbf{u} = (\beta, \delta)$ for C0 and $\mathbf{u} = (\beta, \delta, \theta_F)$ for C4. Linearising about straight sailing, the hydrodynamic side force and yaw moment are $\mathbf{A}\mathbf{u}$ with $\mathbf{A} = \partial(Y, N)/\partial \mathbf{u} \in \mathbb{R}^{2\times n}$, and the side-force cost—the increase of the surge resistance relative to straight-ahead sailing, including the course-projection term $Y\sin\beta$—is the quadratic form $\Delta R = 1/2\, \mathbf{u}^{\mathsf{T}}\mathbf{H}\mathbf{u}$. Equilibrium requires $\mathbf{A}\mathbf{u} = -F\,\mathbf{b}$ with $\mathbf{b} = (1, x_A L)^{\mathsf{T}}$.

Proposition 1 (Minimum side-force cost). *If* $\mathbf{H}$ *is positive definite and* $\mathbf{A}$ *has full row rank, the minimum of* ΔR *subject to*

$$\mathbf{A}\mathbf{u} = -F\mathbf{b} \;\; \text{is} \;\; D^* = 1/2\, F^2\, \mathbf{b}^{\mathsf{T}}\mathbf{M}^{-1}\mathbf{b} = \frac{F^2}{2K}\left[1 + \left(\frac{x_A - \bar{x}}{\sigma}\right)^2\right], \qquad \mathbf{M} = \mathbf{A}\mathbf{H}^{-1}\mathbf{A}^{\mathsf{T}}, \tag{14}$$

with the side-force conductance $K = M_{11}$*, the hydrodynamic centre* $\bar{x} = M_{12}/(M_{11}L)$ *and the lever spread* $\sigma = \sqrt{\det\mathbf{M}}/(M_{11}L)$.

Proof. Stationarity of $1/2\, \mathbf{u}^{\mathsf{T}}\mathbf{H}\mathbf{u} + \boldsymbol{\lambda}^{\mathsf{T}}(\mathbf{A}\mathbf{u} + F\mathbf{b})$ gives $\mathbf{u}^* = -\mathbf{H}^{-1}\mathbf{A}^{\mathsf{T}}\boldsymbol{\lambda}$ and $\boldsymbol{\lambda} = F\mathbf{M}^{-1}\mathbf{b}$, hence $D^* = 1/2\, F^2 \mathbf{b}^{\mathsf{T}}\mathbf{M}^{-1}\mathbf{b}$. Writing the inverse of the symmetric 2×2 matrix explicitly, $\mathbf{b}^{\mathsf{T}}\mathbf{M}^{-1}\mathbf{b} = (M_{22} - 2M_{12}x_A L + M_{11}x_A^2 L^2)/\det\mathbf{M}$; completing the square in x_A yields Eq. (14).

The first factor, $F^2/2K$, is the cost of side force alone. It generalises Munk's result that the induced drag of a system of lifting elements depends only on their combined efficiency [21]. The bracket is a moment penalty that grows quadratically with the distance between the sail centre of effort and the hydrodynamic centre $\bar{x}$, measured in units of σ.

Corollary 1 (Independent lifting elements). *If each element* i *is driven by its own control,* $Y_i = g_i u_i$ *acting at* x_i*, with cost* $Y_i^2/(2k_i)$*, then* $K = \sum_i k_i$*,* $\bar{x} = \sum_i k_i x_i/K$ *and* $\sigma^2 = \sum_i k_i (x_i - \bar{x})^2/K$*: the conductance-weighted sum, centroid and variance of the element positions. Adding an adjustable fin of conductance* k_F *at* x_F *removes the moment penalty when* $x_F = x_A + (K_0/k_F)(x_A - \bar{x}_0)$.

Corollary 2 (Fin break-even side force). *Let a deployed fin add the zero-lift drag* D_{F0} *and change the invariants from* $(K_0, \bar{x}_0, \sigma_0)$ *to* $(K_1, \bar{x}_1, \sigma_1)$*. Deployment lowers the total cost if and only if*

$$F > F_{\text{crit}} = \sqrt{\frac{2D_{F0}}{\Phi_0 - \Phi_1}}, \qquad \Phi_j = \frac{1}{K_j}\left[1 + \left(\frac{x_A - \bar{x}_j}{\sigma_j}\right)^2\right]. \tag{15}$$

Proposition 2 (Yaw-balance capacity). *With actuator limits* $|\delta| \le \delta_{\max}$, $|\theta_F| \le \theta_{\max}$, $|\delta_f| \le \delta_{f,\max}$ *and* $|\beta| \le \beta_{\max}$*, the largest side force that can be balanced is the linear programme*

$$F_{\max}(x_A) = \max\{F:\ \mathbf{A}\mathbf{u} + F\mathbf{b} = \mathbf{0},\ \mathbf{u} \in \mathcal{U}\}. \tag{16}$$

For the two-element system C0, $\mathbf{u} = -F\mathbf{A}^{-1}\mathbf{b}$ *and* $F_{\max} = \delta_{\max}/|\mathbf{e}_\delta^{\mathsf{T}}\mathbf{A}^{-1}\mathbf{b}|$.

Proposition 2 separates two roles of an appendage. A fin or flap that barely changes K can still enlarge $F_{\max}$ considerably, because it adds a yaw-moment actuator or increases the rudder lift attainable within $\delta_{\max}$. When F exceeds $F_{\max}$, the sails must be depowered, and the lost sail thrust then dominates the side-force cost.

4.2 Numerical Solution

Problem (4) is solved with sequential quadratic programming (SLSQP) for each configuration and deployment state. To avoid local minima the optimiser is seeded with the maximum-thrust sail trim, with two partially feathered trims and with generic trims of both signs, and it is stopped after two feasible solutions have been found; equality residuals are scaled by $1/2\,\rho V^2 Ld$ and required below 10^{-6}. The sail-first baseline trims the sails for maximum thrust at zero leeway, then optimises the hydrodynamic controls; if yaw balance is infeasible, the sails are depowered along the feathering path by bisection. All 1.6×10^4 table optimisations reported below converged.

5 DATA AND EXPERIMENTAL DESIGN

5.1 Ship, Devices and Rig

Table 3 lists the appendage and rig parameters. The baseline fin is a slim daggerboard of 8 m span and 6 m chord at $x_F = -0.30L$, near the aft end of the parallel middle body; its effective aspect ratio with the hull image is 2.67, the load-weighted up-wash factor is $\kappa_F = 1.60$ and the boundary-layer pressure factor is 0.95. The flap rudder has the area, span and chord of the KVLCC2 rudder and a 30% flap.

Table 3 Appendage and Rig Parameters (Baseline)

Item	Parameter	Value
Rudder	section, flap chord	NACA 0018, $c_f/c = 0.3$ (0.2, 0.4 studied)
	area, span, chord, Λ	112.6 m², 15.8 m, 7.13 m, 2.22
	$C_{L\alpha}$ (anchored)	$f_\alpha = 2.747$ rad⁻¹
Fin	section, span×chord	NACA 0015, 8×6 m (4–10 m span studied)
	position, Λ_e, $C_{L\alpha}$	$x_F = -0.30L$ (-0.40 to $+0.15L$ studied), 2.67, 3.08 rad⁻¹
	κ_F, q_F/q_∞	1.60, 0.95
Sails	number, span×chord	4, 50×20 m, NACA 0018 with 30% flap
	$A_S/(Ld)$, x_A, z_c	0.60 (0.3–1.2 studied), $0.02L$, 37.2 m
Operation	speed, helm limit	12 kn (8–14 kn), $\delta_{\max} = 10°$ (5–15°)

5.2 Real Wind Data and Route

Two independent real wind records are used. The first is the continuous-wind record of NOAA NDBC station 46002 in the open north-east Pacific off Oregon [22]: 28 468 ten-minute observations of speed and direction from 31 December 2015 to 18 July 2016. The anemometer speeds are converted to 10 m with the 0.11 power law [20], assuming an anemometer height of 4.1 m. The second is the NREL WIND Toolkit [23]: 8 760 hourly values of 10 m wind speed and direction for 2019 at the offshore grid point 40.74°N, 124.54°W off Cape Mendocino. Both records were obtained from the example data of the open-source MHKiT-Python toolkit [24]. Mean 10 m wind speeds are 8.06 and 6.78 m/s, and winds above 12 m/s occur 14.0% and 12.0% of the time, respectively.

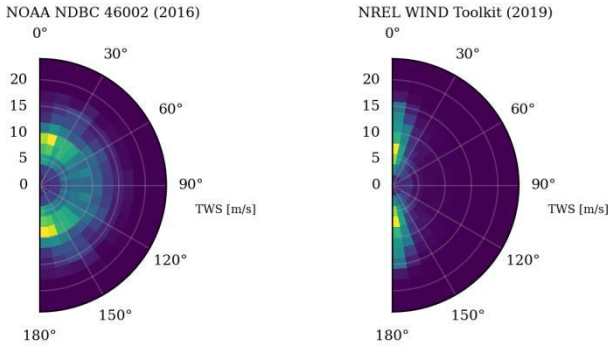


Figure 2 Joint Distribution of True Wind Speed and $|\mathrm{TWA}|$ on the North–South Route for the NDBC 46002 Observations (Left) and the NREL WIND Toolkit Record (Right)

Both records are applied to a north–south coastal tanker trade with courses of 165° (southbound) and 345° (northbound), each sailed half of the time; the true wind angle is TWA = $\theta_{\text{wind}} - \chi_{\text{course}}$, wrapped to $(-180^\circ, 180^\circ]$. Figure 2 shows the resulting joint distributions. The WIND Toolkit point is dominated by along-coast winds that arrive close to the bow or stern, whereas the buoy record contains more reaching angles.

5.3 Performance Tables and Route Metric

For each configuration, speed and scenario, Problem (4) is solved on a grid of $U_{10} \in \{0,3,6,9,12,15,18,22\}$ m/s and TWA $\in \{-180^\circ, -165^\circ, ..., 165^\circ\}$ (192 conditions; both tacks, because γ_R is asymmetric). The relative power $P_D/P_{D,\text{ref}}$ is interpolated bilinearly (periodically in TWA) to every wind record, and the route saving is

$$S = 1 - \frac{1}{N}\sum_{j=1}^{N} \frac{P_D(U_{10,j},\text{TWA}_j)}{P_{D,\text{ref}}}, \tag{17}$$

where $P_{D,\text{ref}}$ is the delivered power of the same ship without sails and fin (5.87 MW at 10 kn and 9.90 MW at 12 kn). Differences between configurations are reported in percentage points (pp).

5.4 Experimental Protocol

The experiments comprise: (E1) validation of the section, lifting-surface and up-wash models; (E2) verification of Propositions 1–2 against the non-linear optimum, with the sails replaced by a pure side force F at x_A; (E3) route-level comparison of C0–C5 and of the sail-first baseline at 10 and 12 kn; (E4) eleven regime scenarios varying $\delta_{\max}$, $A_S/(Ld)$, x_A and V; (E5) a wind-dominant design case ($A_S/(Ld) = 1.2$, 10 kn, $\delta_{\max} = 5^\circ$) with a fin design map ($s_F \in \{4,6,8,10\}$ m, $x_F/L \in \{-0.40, -0.30, -0.15, 0, 0.15\}$), flap-chord ratios and linkage ratios; (E6) ablation of the up-wash, boundary-layer immersion, γ_R asymmetry, fin–rudder vortex, independent flap control, propeller unloading and joint optimisation; and (E7) robustness to the section-data source (NeuralFoil instead of XFOIL), to the wind dataset, and to joint uniform perturbations of 12 uncertain parameters in a 30-sample Monte Carlo study: Y'_v, Y'_{vvv} and N'_v, N'_{vvv} ($\pm 10\%$), X'_{vv} ($\pm 30\%$), f_α ($\pm 10\%$), γ_R, t_R, a_H ($\pm 15\%$), $\kappa_F \in [1.0, 1.8]$, a fin–hull lift carry-over factor $a_F \in [0, 0.3]$, the fin profile drag ($\times [0.8, 1.3]$), the flap effectiveness ($\pm 15\%$) and the sail lift slope ($\pm 10\%$).

6 RESULTS

6.1 Validation of the Appendage Model

Figure 3 and Table 4 summarise the section-level results. XFOIL and NeuralFoil agree within 0.2% in lift slope and 0.8% in maximum lift for all four sections, and within 4% in minimum drag. At small deflections the XFOIL flap effectiveness of the 30% flap ($\tau = 0.66$–0.73 for $\delta_f \leq 15^\circ$) matches thin-airfoil theory ($\tau = 0.661$). Above 20° it falls to $\tau = 0.47$ at 30° as the flow over the deflected flap separates, a viscous loss that NeuralFoil does not reproduce ($\tau \approx 0.75$). The XFOIL polars are therefore used for all design results, and NeuralFoil serves as an upper-effectiveness alternative in the robustness study. For a full-span flap the VLM gives a ratio of flap to angle-of-attack effectiveness of 0.695, within 5% of the two-dimensional thin-airfoil value. This supports transferring the two-dimensional zero-lift shift to the three-dimensional surface in Eq. (9).

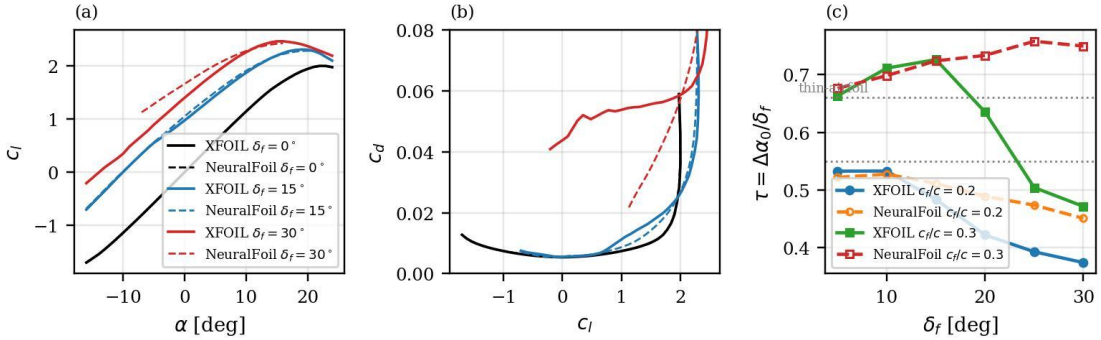


Figure 3 (a) Lift Curves and (b) Drag Polars of the NACA 0018 Rudder Section with a 30% Flap at $Re = 3 \times 10^7$ (XFOIL Solid, NeuralFoil Dashed); (c) Flap Effectiveness $\tau = \Delta\alpha_0/\delta_f$ Compared with Thin-Airfoil Theory

Table 4 Validation Metrics of the Section and Low-Aspect-Ratio Models

Quantity	Present model	Reference
a_0 NACA 0015, $Re = 2.7 \times 10^6$	6.43 rad^{-1} (XFOIL)	6.44 (NeuralFoil)
$c_{d,\min}$ NACA 0015	0.0056	0.0057 (NeuralFoil)

Quantity	Present model	Reference
$c_{l,\max}$ NACA 0015	1.650	1.662 (NeuralFoil)
$C_{L\alpha}$ at $\Lambda_e = 1,2,3$	1.50, 2.58, 3.31 rad^{-1}	1.49, 2.62, 3.40 (Helmbold)
RMS ΔC_L, $\alpha \le 16°$, $\Lambda_e = 1,2,3$	0.017, 0.022, 0.028	DTMB correlation [19]
RMS ΔC_D, $\alpha \le 16°$, $\Lambda_e = 1,2,3$	0.0008, 0.0010, 0.0006	DTMB correlation [19]
τ, 30% flap, $\delta_f \le 15°$	0.66–0.73	0.661 (thin airfoil)
3-D/2-D full-span flap ratio	0.695 (VLM)	0.661 (thin airfoil)

Figure 4 compares the low-aspect-ratio model with the Whicker–Fehlner (DTMB) correlations, which were derived from wind-tunnel tests of NACA 0015 control surfaces with effective aspect ratios of 1–3 [19]. The section-corrected VLM lift slope lies within -2.9% to $+2.7\%$ of the Helmbold relation over $\Lambda_e = 0.5$–6. It is 5–9% above the DTMB slope, which assumes a reduced section slope $0.9 \times 2\pi$; Prandtl's lifting line overestimates the slope by 25–60% at these aspect ratios. Over $\alpha \le 16°$ the predicted C_L and C_D curves follow the DTMB correlations with RMS deviations of 0.017–0.028 and 0.0006–0.0010, and the maximum relative lift deviation is 5.4–7.2%. Figure 5 shows the hull up-wash: the lateral velocity at the keel is 1.72 times the cross-flow and decays with depth, giving load-weighted factors $\kappa_F = 1.55$–1.68 for spans of 2–12 m, while boundary-layer immersion lowers the fin dynamic pressure by 19% for a 2 m fin and by 5% for the 8 m baseline.

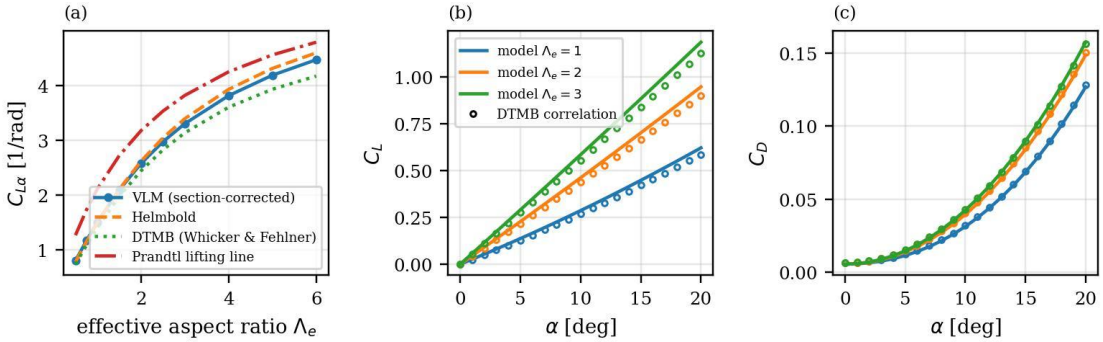


Figure 4 Low-Aspect-Ratio Validation for NACA 0015 Surfaces (Taper 0.45, Square Tips, $Re = 2.7 \times 10^6$): (a) Lift Slope versus Effective Aspect Ratio; (b) Lift and (c) Drag Coefficients of the Present Model (Lines) against the DTMB Correlation (Symbols)

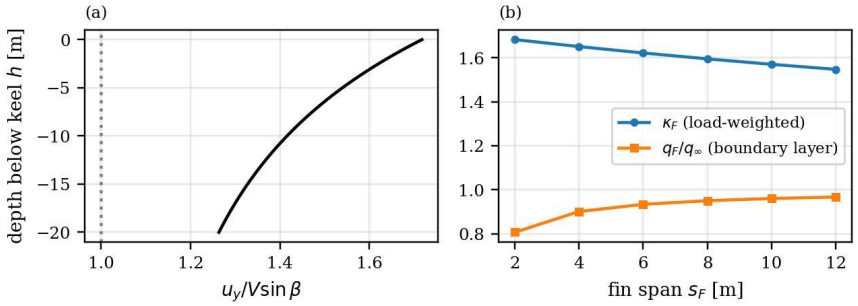


Figure 5 (a) Potential-Flow Lateral Velocity below the KVLCC2 Midship Double-Body Section; (b) Load-Weighted Up-Wash Factor κ_F and Boundary-Layer Pressure Factor versus Fin Span at $x_F = -0.30L$, 12 kn

6.2 Verification of the Allocation Theory

The hydrodynamic invariants of the KVLCC2 at 12 kn, obtained from the Jacobian and Hessian of the full model, are $K_0 = 26.56$ MN, $\bar{x}_0 = 0.0054L$ and $\sigma_0 = 0.632L$ for hull and rudder. With the baseline fin they become $K_1 = 28.48$ MN, $\bar{x}_1 = 0.0030L$ and $\sigma_1 = 0.610L$. Although the hull centre of lateral resistance lies at $0.44L$, the hydrodynamic centre is close to midship: the rudder, whose side force is amplified by the hull–rudder interaction ($a_H = 0.312$) while its drag is reduced by $(1 - t_R)$, is an efficient side-force producer at the stern. The large lever spread then makes the moment penalty small for centres of effort near midship.

Figure 6a compares Eq. (14) with the non-linear optimum for a pure side force at $x_A = 0.02L$. For C0 the closed form is within 1.7% for $F \le 3$ MN (18.8 versus 19.2 kN at 1 MN; 117.7 versus 118.2 kN at 2.5 MN). For C4 the numerical cost equals Eq. (14) plus the fin zero-lift drag $D_{F0} = 4.66$ kN, again within 1.2%. The sweep over the centre of effort (Figure

6b) reproduces the quadratic moment penalty, with the minimum at $x_A \approx \bar{x}$. Equation (15) predicts a fin break-even side force of 1.92 MN; the numerical cost curves of C0 and C4 cross at 1.88 MN.

The side-force cost itself is small: 1 MN, about 0.9 times the calm-water resistance at 12 kn, costs 19 kN (1.7% of R_T) and requires 0.77° of leeway. The helm, however, grows linearly at 3.97° per MN (Figure 6c). At 3 MN the conventional rudder needs 11.1°, while the flap rudder holds 5.5° with an 8° flap. The binding constraint is therefore the yaw-balance capacity (Figure 7). With $\delta_{\max} = 5^\circ$ and $x_A = 0$, C0 balances 1.20 MN, the adjustable fin raises this to 2.16 MN and the flap rudder to 6.02 MN. Moving the centre of effort aft to $x_A = -0.2L$ reduces the three capacities to 0.78, 1.34 and 3.35 MN. The linear programme of Proposition 2 predicts the C0 and C4 capacities within 3.3% wherever they are bounded. With a secant flap column it underestimates the flap-rudder capacity by 10–26%, because the viscous flap effectiveness is non-linear.

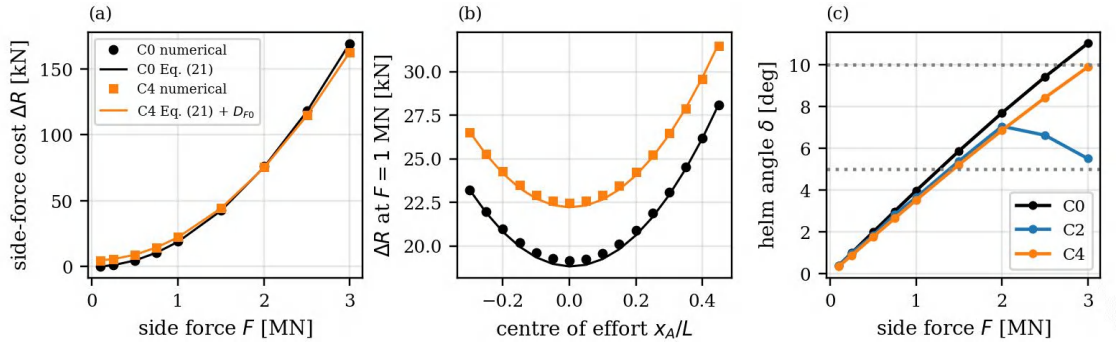


Figure 6 Verification of the Allocation Theory at 12 kn: (a) Side-Force Cost versus Side Force; (b) Cost at $F = 1$ MN versus Centre of Effort; (c) Helm Angle versus Side Force for C0, C2 and C4 (Dotted Lines: 5° and 10° Helm Limits)

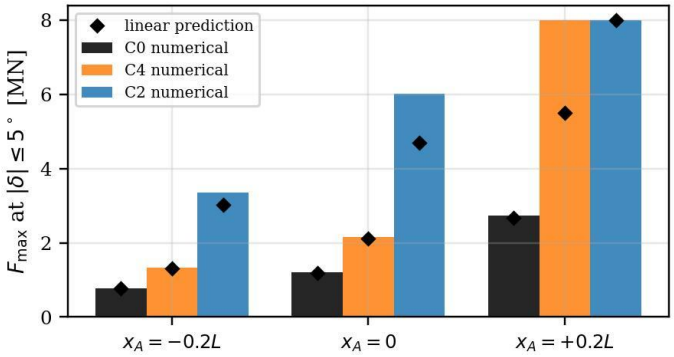


Figure 7 Yaw-Balance Capacity $F_{\max}$ with a 5° Helm Limit: Non-Linear Model (Bars, Capped at the 8 MN Search Limit) and Linear Prediction of Proposition 2 (Diamonds)

6.3 Route-Level Performance of the Baseline Ship

Table 5 lists the route savings. The baseline wind-assisted ship saves 23.06% of the propulsive energy on the north–south route with the buoy winds and 6.36% with the WIND Toolkit winds at 12 kn. At 10 kn the savings are 30.34% and 9.28% for C0, and 30.45, 30.44 and 30.46% (NDBC) and 9.30% (WIND Toolkit) for C2, C4 and C5 with optimal deployment. The difference between the datasets reflects the alignment of the dominant along-coast winds with the route at Cape Mendocino. Joint optimisation of sail trim and hydrodynamic controls adds 0.17 pp (NDBC) and 0.07 pp (WIND Toolkit) relative to sail-first trimming.

Table 5 Route-Level Energy Savings S (%) at 12 kn with $\delta_{\max} = 10^\circ$, Mean Helm and Fraction of Time with $|\delta| \geq 8^\circ$ (NDBC). "opt." denotes the optimal fin deployment policy.

Configuration	S NDBC	S WIND Toolkit	mean $\lvert\delta\rvert$ (°)	$\lvert\delta\rvert \geq 8^\circ$ (%)
C0 sail-first	22.89	6.29	–	–
C0	23.06	6.36	1.75	1.96
C1 flap linked	23.07	6.36	1.07	0.07
C2 flap free	23.07	6.36	1.57	0.35
C3 deployed / opt.	22.62 / 23.08	5.87 / 6.36	1.63	1.59
C4 deployed / opt.	22.65 / 23.10	5.88 / 6.36	1.53	1.25
C5 deployed / opt.	22.69 / 23.08	5.88 / 6.36	1.35	0.06

At this sail intensity, all appendage options change the annual saving by less than 0.05 pp, because the helm limit is active less than 2% of the time. The devices instead change how the side force is balanced. The flap rudder reduces the time spent at or above 8° helm from 1.96% to 0.07–0.35%. A permanently deployed fin costs 0.41–0.49 pp of saving through its profile drag, which is recovered by the retraction policy (deployed 2–6% of the time). Figure 8 shows the condition-level picture: reaching conditions at 15 m/s require 8–10° helm with the conventional rudder and about half of that with a flap rudder, at practically equal power.

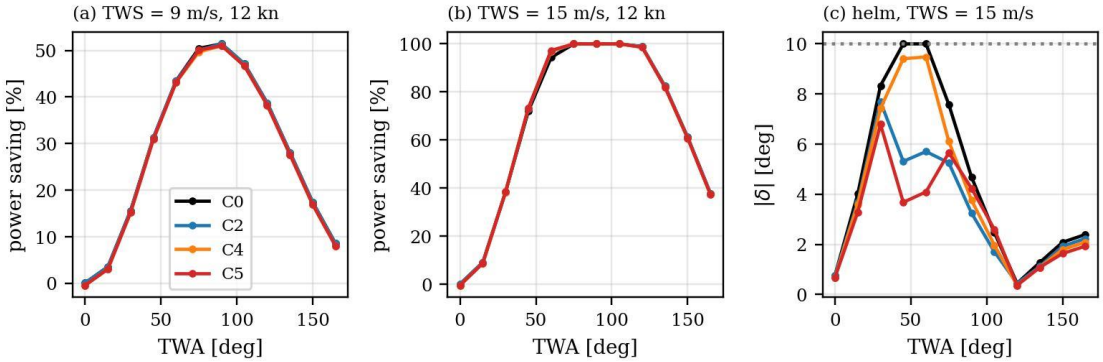


Figure 8 Baseline Ship at 12 kn: Power Saving versus TWA at (a) 9 m/s and (b) 15 m/s, and (c) Helm Angle at 15 m/s

6.4 Operating Regimes

Table 6 and Figure 9 show how the benefit of the devices depends on the operating regime. Each benefit is the change in annual saving relative to C0 with the buoy winds. The benefit grows with every factor that tightens the yaw balance. Reducing the helm limit to 5° raises the flap-rudder benefit to 0.66 pp and that of the combined system to 0.67 pp; a sail-area ratio of 1.2 gives 0.41 and 0.44 pp. Slow steaming at 8 kn, which lowers the hydrodynamic dynamic pressure while the sail loads remain, gives 0.38 and 0.41 pp, and moving the centre of effort to $-0.15L$ gives 0.18 and 0.19 pp. Conversely, a forward centre of effort ($+0.15L$), a higher speed (14 kn) or a smaller rig ($A_S/(Ld) = 0.3$) leave the yaw balance unconstrained and the benefits vanish. A permanently deployed fin pays only in the three most demanding scenarios, which agrees with the break-even logic of Corollary 2.

Table 6 Regime Study (NDBC Winds): Baseline Saving of C0, Change in Saving of C2, C4 and C5 with Optimal Deployment and of C4 Permanently Deployed (pp), and Mean Helm of C0

Scenario	S_{C0} (%)	ΔC2	ΔC4 opt.	ΔC5 opt.	ΔC4 dep.	$\lvert\delta\rvert_{C0}$ (°)
Baseline	23.06	0.007	0.038	0.019	-0.412	1.75
$\delta_{max} = 15^\circ$	23.07	0.002	0.005	0.005	-0.415	1.76
$\delta_{max} = 7.5^\circ$	22.92	0.154	0.136	0.157	-0.281	1.69
$\delta_{max} = 5^\circ$	22.41	0.662	0.554	0.665	0.158	1.56
$A_S/(Ld) = 0.3$	12.61	0.000	0.000	0.000	-0.478	0.84
$A_S/(Ld) = 0.9$	30.68	0.215	0.200	0.232	-0.160	2.48
$A_S/(Ld) = 1.2$	36.25	0.411	0.362	0.441	0.045	3.07
$x_A = +0.15L$	23.05	0.001	0.003	0.003	-0.420	1.10
$x_A = -0.05L$	22.98	0.085	0.077	0.088	-0.341	1.96
$x_A = -0.15L$	22.84	0.182	0.134	0.187	-0.279	2.39
$V = 14$ kn	17.81	0.010	0.009	0.010	-0.445	1.39
$V = 8$ kn	39.84	0.377	0.332	0.405	0.035	2.99

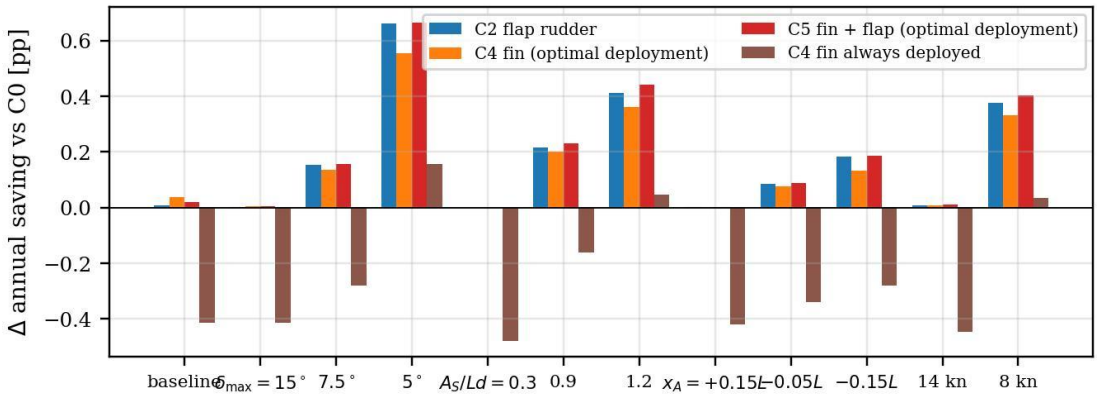


Figure 9 Change in Annual Saving Relative to C0 across Operating Regimes (NDBC Winds)

6.5 Wind-Dominant Design Case

The wind-dominant case combines the three main drivers: $A_S/(Ld) = 1.2$, 10 kn and $\delta_{max} = 5°$. Its results are given in Table 7 and Figure 10. With the buoy winds, C0 saves 40.01%. The linked flap rudder adds 3.07 pp, the independently controlled flap rudder 4.66 pp and the adjustable fin 3.29 pp, or 3.52 pp with optimal deployment (deployed 38.9% of the time). The combined system C5 adds 4.50 pp permanently deployed and 4.77 pp with optimal deployment, its fin being used only 15.7% of the time. The fixed fin (C3) adds only 0.25 pp, or 0.49 pp with deployment control, because without incidence control its lift is tied to the small leeway. With the WIND Toolkit winds the ranking is identical at smaller magnitudes (C2 +1.68 pp, C4 +1.24 pp, C5 +1.70 pp on a 14.41% baseline).

The condition-level results (Figure 10a) show where the benefit arises. At 12 m/s and TWA = $30–75°$ the conventional rudder reaches its helm limit and the sails must be partly depowered. The flap rudder and the fin restore full sail power, which raises the saving at TWA = $45°$ from 55% to almost 100%. Figure 10b–c shows the allocation at 9 m/s: with C0 the hull carries 55% and the rudder 45% of the hydrodynamic side force at all angles. With C5 the adjustable fin takes 10–17% at the expense of the rudder, while the hull share remains close to 53%.

Table 7 Wind-Dominant Design Case ($A_S/(Ld) = 1.2$, 10 kn, $\delta_{max} = 5°$): Change in Annual Saving Relative to C0 (pp), Fraction of Time the Fin Is Deployed under the Optimal Policy and Mean Helm (NDBC). Absolute C0 savings: 40.01% (NDBC) and 14.41% (WIND Toolkit).

Config.	ΔS deployed	ΔS opt.	deployed (%)	mean $\lvert\delta\rvert$ (°)	ΔS opt. (WTK)
C0	–	–	–	2.61	–
C1	3.07	–	–	2.02	1.13
C2	4.66	–	–	1.90	1.68
C3	0.25	0.49	35.0	–	0.13
C4	3.29	3.52	38.9	2.45	1.24
C5	4.50	4.77	15.7	1.98	1.70

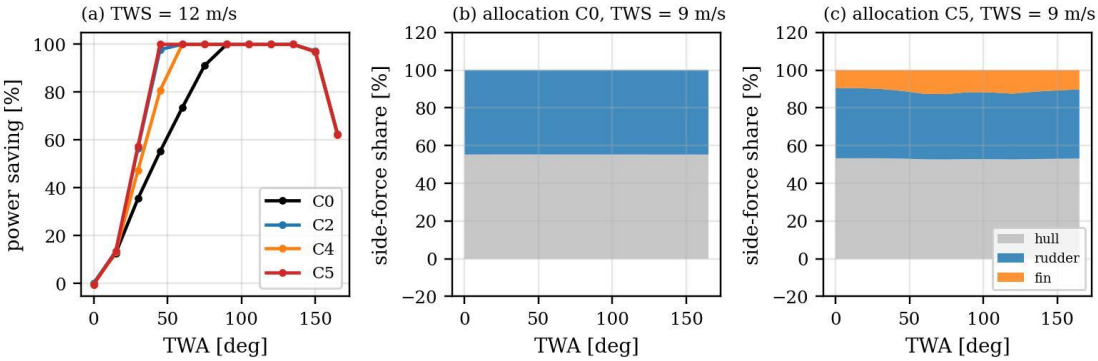


Figure 10 Wind-Dominant Case: (a) Power Saving versus TWA at 12 m/s; Side-Force Allocation among Hull, Rudder and Fin at 9 m/s for (b) C0 and (c) C5

6.6 Fin and Flap-Rudder Design

Figure 11 maps the annual benefit of the adjustable fin over span and position in the wind-dominant case. For spans of 6–10 m the benefit increases monotonically as the fin moves aft. A 10 m fin gives 4.55 pp at $x_F = -0.40L$ and 2.48 pp at midship, and an 8 m fin gives 3.91 pp at $-0.40L$ and 3.52 pp at the baseline $-0.30L$. This follows Corollary 1: the fin

acts mainly as a yaw-moment actuator, and its moment arm about the hydrodynamic centre ($\bar{x} \approx 0$) grows aft. Forward of midship the fin has little authority; a permanently deployed 8 m fin at $+0.15L$ even loses 0.33 pp. The always-deployed map (Figure 11b) is uniformly lower, by 0.1–0.6 pp, which quantifies the value of retraction.

For the flap rudder, flap-chord ratios of 0.2, 0.3 and 0.4 give 4.57, 4.66 and 4.72 pp, so the benefit saturates beyond 30% chord. The linkage ratio matters more. A linked flap with $\delta_f = k\delta$ gives 1.95, 3.07, 3.81 and 4.27 pp for $k = 0.5$, 1.0, 1.5 and 2.0, approaching the 4.66 pp of independent control only for strongly geared linkages. In helm-limited operation the flap is the actuator that supplies lift beyond the helm limit, so its authority should not be tied to the helm angle.

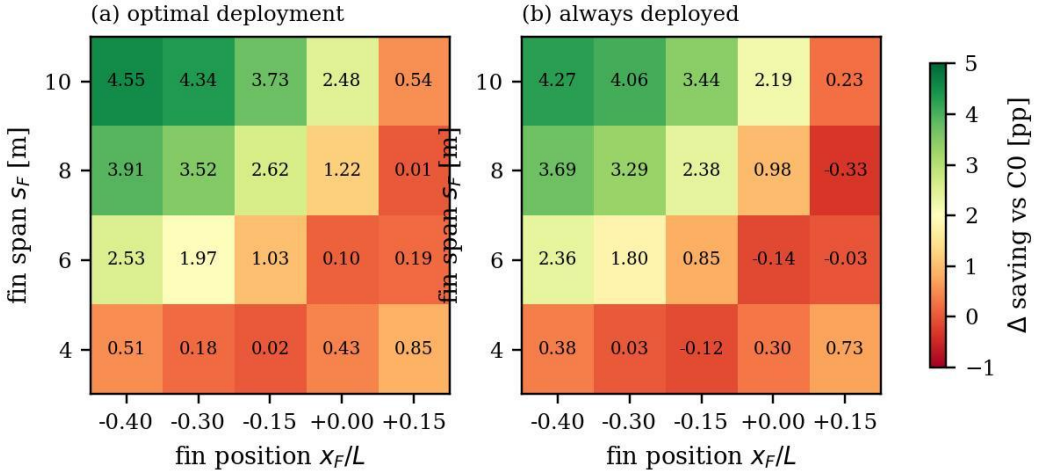


Figure 11 Change in Annual Saving of the Adjustable Fin (C4) Relative to C0 over Fin Span and Position in the Wind-Dominant Case: (a) Optimal Deployment; (b) Permanently Deployed

6.7 Ablation and Robustness

Table 8 and Figure 12a report the ablation study for the full system (C5 with optimal deployment, 44.78% saving in the wind-dominant case). Three model elements matter. The first is propeller unloading. Holding the rudder slipstream at the straight-ahead loading overstates the C0 saving by 2.03 pp (42.05% instead of 40.01%), because it keeps the rudder artificially strong when the sails take over thrust. This underestimates the device benefit by 41% (2.81 instead of 4.77 pp). The second is joint optimisation: sail-first trimming with bisection depowering reaches 43.95%, 0.83 pp below the joint optimum, and depowers the sails by 7.4% on average. The third is independent flap control, whose replacement by a linked flap costs 0.11 pp. The fin–rudder vortex interaction reduces the saving by 0.09 pp, because the fin sidewash lowers the rudder inflow angle. Up-wash, boundary-layer immersion and the γ_R asymmetry change the annual result by less than 0.01 pp: with adjustable incidence the fin loading is set by θ_F rather than by the local cross-flow.

Table 8 Ablation and Robustness in the Wind-Dominant Case (NDBC Winds)

Variant	S (%)	change (pp)
Full model, C5 with optimal deployment	44.78	–
No hull up-wash ($\kappa_F = 1$)	44.78	0.00
No boundary-layer immersion	44.78	0.00
Symmetric γ_R	44.78	0.00
No fin–rudder vortex interaction	44.87	*+0.09*
Linked instead of independent flap	44.67	*−0.11*
No propeller unloading (C5 / C0)	44.86 / 42.05	*+0.08 / +2.03*
Sail-first trimming (decoupled)	43.95	*−0.83*
NeuralFoil: S_{C0} / ΔC2 / ΔC5 dep.	39.75 / 4.80 / 4.59	–
Monte Carlo ($n = 30$): ΔC2	*4.70 ± 0.55*	5–95%: 3.76–5.58
Monte Carlo ($n = 30$): ΔC4 opt.	*3.99 ± 0.50*	5–95%: 3.17–4.77
Monte Carlo ($n = 30$): ΔC5 opt.	*4.83 ± 0.56*	5–95%: 3.87–5.72

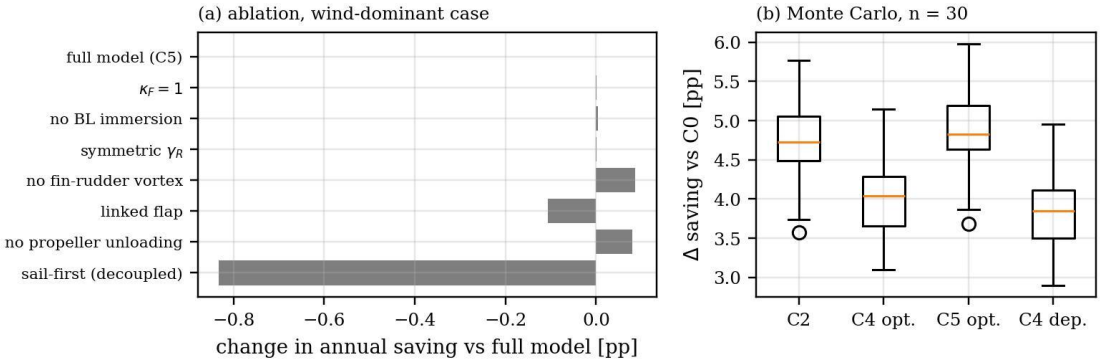


Figure 12 (a) Ablation of Model Elements for the Full System in the Wind-Dominant Case; (b) Monte Carlo Distributions of the Change in Annual Saving Relative to C0 for Joint Perturbations of 12 Uncertain Parameters

The conclusions are robust to the main sources of model uncertainty. With NeuralFoil polars, the C0 saving changes by -0.26 pp and the device benefits by $+0.14$ (C2) and $+0.09$ pp (C5 deployed). Under the joint Monte Carlo perturbations, the baseline saving is 39.88 ± 0.52% and the benefits are 4.70 ± 0.55 pp (C2), 3.99 ± 0.50 pp (C4) and 4.83 ± 0.56 pp (C5). Every sample yields a positive flap-rudder benefit, and the combined system is never worse than the flap rudder alone (Figure 12b). The second wind dataset preserves the ranking C5 ≥ C2 > C4 > C3.

7 DISCUSSION

The results separate two hydrodynamic functions that are often conflated in the assessment of anti-leeway devices: reducing the cost of side force and providing yaw-balance capacity. For a full-form ship such as the KVLCC2, the hull is an efficient lifting body and the rudder, assisted by hull–rudder interaction, completes an appendage system with a hydrodynamic centre near midship and a large lever spread. The cost of side force is then small—19 kN per (MN)² at 12 kn—and a fin adds only 7% to the conductance K. A fin therefore cannot pay through drag reduction alone, and Corollary 2 places its break-even side force near 1.9 MN. This is consistent with the observation that the rudder is the main source of sail-induced resistance and that only a dynamically controlled keel improved the savings of a wind-powered cargo ship [8]. It also agrees with the experimental finding that appendages placed to counter the destabilising yaw moment are the effective ones [6].

The capacity function dominates whenever the yaw balance binds. Four drivers make this happen: a tight helm limit, a large sail area relative to the lateral area, slow steaming, and a centre of effort aft of the hydrodynamic centre. The rudder's capacity also shrinks as the propeller unloads. In this regime the flap rudder is the most effective single device, because it raises the attainable rudder lift at fixed helm without adding wetted area. An adjustable, retractable fin placed well aft provides a comparable but smaller benefit and complements the flap rudder. Based on the quantitative evidence above, four design guidelines follow.

1. Use Eq. (14) and Proposition 2 at the concept stage: compute $(K, \bar{x}, \sigma)$ from manoeuvring coefficients and compare the expected side force with $F_{\max}$ at the intended helm limit.
2. Give priority to a flap rudder with independent (or strongly geared) flap control when F approaches $F_{\max}$; flap-chord ratios beyond 0.3 add little.
3. Install an anti-leeway fin only with incidence control and retraction, as far aft as the hull form allows; a fixed fin or a fin forward of midship is not effective for this hull form.
4. Optimise sail trim jointly with the hydrodynamic controls and model propeller unloading in the rudder inflow; both affect the predicted saving by more than the choice of appendage in most regimes.

The analysis covers steady sailing in calm water with three degrees of freedom and a common sail trim. Extending it to seaway-induced added resistance, dynamic course keeping and sail–sail interaction is a natural next step. The allocation invariants $(K, \bar{x}, \sigma)$ can be identified directly from captive or free-running model tests. This makes the theory equally applicable to ship types with smaller lateral area and forward-located rigs, where the yaw balance and the side-force cost are expected to differ from the full-form tanker studied here.

8 CONCLUSIONS

A moment-constrained side-force allocation framework has been developed for wind-assisted merchant ships and applied to the KVLCC2 with four wing sails, retractable anti-leeway fins and flap rudders. The main conclusions are as follows.

1. The minimum side-force cost has the closed form $D^* = F^2/(2K)\left[1 + \left((x_A - \bar{x})/\sigma\right)^2\right]$, with three invariants computable from manoeuvring coefficients. It agrees with the non-linear optimum within 1.7% and predicts the fin break-even side force within 2.1%.
2. The low-aspect-ratio appendage model reproduces the DTMB control-surface correlations with RMS lift deviations of 0.017–0.028. Its viscous flap effectiveness matches thin-airfoil theory at small deflections and captures the loss at large deflections.

3. For the KVLCC2 the hydrodynamic centre lies near midship ($\bar{x} = 0.005L$) despite the forward centre of lateral resistance, and the cost of side force is small (1.7% of the calm-water resistance per MN at 12 kn). The yaw-balance capacity under the helm limit is the binding constraint.

4. With real wind statistics at a sail-area ratio of 0.6, 12 kn and a 10° helm limit, appendages change the annual saving by less than 0.05 pp. The flap rudder cuts the time above 8° helm from 1.96% to 0.35%, and a permanently deployed fin costs about 0.4–0.5 pp.

5. In the wind-dominant case ($A_S/(Ld) = 1.2$, 10 kn, 5° helm limit), the flap rudder adds 4.66 pp, the retractable adjustable fin 3.52 pp and their combination 4.77 pp with the fin deployed 16% of the time. These benefits are robust to section data, wind dataset and parameter uncertainty (4.83 ± 0.56 pp).

6. Propeller unloading and joint sail–hydro optimisation are first-order effects: neglecting the former overstates the baseline saving by 2.0 pp, and sail-first trimming loses 0.83 pp.

COMPETING INTERESTS

The authors have no relevant financial or non-financial interests to disclose.

DATA AVAILABILITY

The wind data are publicly available from NOAA NDBC (station 46002) and the NREL WIND Toolkit [22-23]; the records used were taken from the example data of MHKiT-Python [24]. The KVLCC2 particulars and MMG coefficients are published in [12, 15]. All computed polars, performance tables and route results are provided with the code.

REFERENCES

[1] International Maritime Organization. Resolution MEPC.377(80): 2023 IMO Strategy on Reduction of GHG Emissions from Ships. IMO, London, 2023.

[2] Chou T, Kosmas V, Acciaro M, et al. A comeback of wind power in shipping: an economic and operational review on the wind-assisted ship propulsion technology. Sustainability, 2021, 13(4): 1880. DOI: 10.3390/su13041880.

[3] Tillig F, Ringsberg J W. Design, operation and analysis of wind-assisted cargo ships. Ocean Engineering, 2020, 211: 107603. DOI: 10.1016/j.oceaneng.2020.107603.

[4] Kolk N J, Keuning J A, Huijsmans R H M. Part 1: Experimental validation of a RANS-CFD methodology for the hydrodynamics of wind-assisted ships operating at leeway angles. Ocean Engineering, 2019, 178: 375-387.

[5] Kolk N. Sailing efficiency and course keeping ability of wind assisted ships. PhD thesis, Delft University of Technology, Delft, 2020. DOI: 10.4233/uuid:8707309f-b9a3-4e09-916d-8fb64328a138.

[6] Kolk N J, Akkerman I, Keuning J A, et al. Low-aspect ratio appendages for wind-assisted ships. Journal of Marine Science and Technology, 2021, 26(4): 1126-1143.

[7] Kolk N, Akkerman I, Keuning J A, et al. Dataset: Bilge keels for course stability and sailing efficiency of wind-assisted ships. 4TU.ResearchData, 2019. DOI: 10.4121/uuid:a9314e24-5d4c-4c46-9f99-391ee7cdc1eb.

[8] Kramer J V, Steen S. Sail-induced resistance on a wind-powered cargo ship. Ocean Engineering, 2022, 261: 111688. DOI: 10.1016/j.oceaneng.2022.111688.

[9] Marine Log. Becker launches two new product lines at SMM, 2024. https://www.marinelog.com/technology/becker-launches-two-new-product-lines-at-smm/.

[10] Molland A F, Turnock S R. Marine Rudders and Control Surfaces: Principles, Data, Design and Applications. Butterworth-Heinemann, Oxford, 2007.

[11] Liu J, Hekkenberg R. Sixty years of research on ship rudders: effects of design choices on rudder performance. Ships and Offshore Structures, 2017, 12(4): 495-512.

[12] Yasukawa H, Yoshimura Y. Introduction of MMG standard method for ship maneuvering predictions. Journal of Marine Science and Technology, 2015, 20(1): 37-52. DOI: 10.1007/s00773-014-0293-y.

[13] Mitsuyuki T. ShipMMG.jl: ship maneuvering simulation based on the MMG model, 2021. https://github.com/ShipMMG/ShipMMG.jl.

[14] Holtrop J, Mennen G G J. An approximate power prediction method. International Shipbuilding Progress, 1982, 29(335): 166-170. DOI: 10.3233/ISP-1982-2933501.

[15] Toxopeus S L, Simonsen C D, Guilmineau E, et al. Investigation of water depth and basin wall effects on KVLCC2 in manoeuvring motion using viscous-flow calculations. Journal of Marine Science and Technology, 2013, 18: 471-496. DOI: 10.1007/s00773-013-0221-6.

[16] Drela M. XFOIL: An analysis and design system for low Reynolds number airfoils. In: Mueller T J (ed.) Low Reynolds Number Aerodynamics. Lecture Notes in Engineering, vol. 54. Springer, Berlin, Heidelberg, 1989: 1-12. DOI: 10.1007/978-3-642-84010-4_1.

[17] Sharpe P, Hansman R J. NeuralFoil: An airfoil aerodynamics analysis tool using physics-informed machine learning. arXiv:2503.16323, 2025. DOI: 10.48550/arXiv.2503.16323.

[18] Katz J, Plotkin A. Low-Speed Aerodynamics, 2nd edn. Cambridge University Press, Cambridge, 2001.

[19] Whicker L F, Fehlner L F. Free-stream characteristics of a family of low-aspect-ratio, all-movable control surfaces for application to ship design. Report 933, David Taylor Model Basin, Washington, DC, 1958.

[20] Hsu S A, Meindl E A, Gilhousen D B. Determining the power-law wind-profile exponent under near-neutral stability conditions at sea. Journal of Applied Meteorology, 1994, 33(6): 757-765.
[21] Munk M M. The minimum induced drag of aerofoils. NACA Report 121, National Advisory Committee for Aeronautics, 1923.
[22] National Data Buoy Center. Continuous winds data, station 46002, 2016. NOAA, 2016. https://www.ndbc.noaa.gov/station_page.php?station=46002.
[23] Draxl C, Clifton A, Hodge B-M, et al. The Wind Integration National Dataset (WIND) Toolkit. Applied Energy, 2015, 151: 355-366.
[24] MHKiT-Software. MHKiT-Python: Marine and Hydrokinetic Toolkit. GitHub repository, 2026. https://github.com/MHKiT-Software/MHKiT-Python.